

Deep Plug-and-Play Prior for Low-Rank Tensor Completion

Wen-Hao Xu, Xi-Le Zhao*, Tai-Xiang Jiang*, Yao Wang, and Michael K. Ng

Abstract—Multi-dimensional images, such as color images and multi-spectral images, are highly correlated and contain abundant spatial and spectral information. However, real-world multi-dimensional images are usually corrupted by missing entries. By integrating deterministic low-rankness prior with the data-driven deep prior, we suggest a novel regularized tensor completion model for multi-dimensional image completion. In the objective function, we adopt the newly emerged tensor nuclear norm (TNN) to characterize the global low-rankness prior of the multi-dimensional images. We also formulate an implicit regularizer to plug in the denoising neural network (termed as deep denoiser), which is convinced to express the deep image prior learned from a large number of natural images. The resulting model can be efficiently solved by the alternating directional method of multipliers algorithm under the plug-and-play (PnP) framework. Experimental results on color images, videos, and multi-spectral images demonstrate that the proposed method can recover both the global structure and fine details very well and achieve superior performance over competing methods in terms of quality metrics and visual effects.

Index Terms—Tensor completion, tensor nuclear norm, convolution neural network, alternating direction method of multipliers, plug-and-play framework

I. INTRODUCTION

Due to sensor malfunction and poor atmospheric conditions, there are usually missing values in multi-dimensional images. The image completion problem aims to estimate missing entries from the partially observed entries, which is a fundamental problem in low-level computer vision and computational imaging [1–7].

By exploiting the redundancy of natural images, the image completion problem can be formulated as the following low-rank matrix completion (LRMC) model:

$$\arg \min_{\mathbf{X}} \text{rank}(\mathbf{X}) \quad \text{s.t. } \mathcal{P}_{\Omega}(\mathbf{X}) = \mathcal{P}_{\Omega}(\mathbf{O}), \quad (1)$$

*Corresponding authors. Tel.: +86 28 61831016, Fax: +86 28 61831280.

This work is supported by the National Natural Science Foundation of China (61876203, 61772003, and 11971374), HKRGC GRF (12306616, 12200317, 12300218, and 12300519), China Postdoctoral Science Foundation (2017M610628 and 2018T111031), and the State Key Laboratory of Robotics (2019-O06).

W.-H. Xu, X.-L. Zhao, and T.-X. Jiang are with the Research Center for Image and Vision Computing, School of Mathematical Sciences, University of Electronic Science and Technology of China, Chengdu 611731, P.R.China (e-mails: seanxwh@gmail.com; xlzhao122003@163.com; taixiangjiang@gmail.com; tingzhuhuang@126.com).

Y. Wang is with the School of Management, Xi'an Jiaotong University, Xi'an 710049, China, and also with the State Key Laboratory of Robotics, Shenyang Institute of Automation, Chinese Academy of Sciences, Shenyang 110016, China (e-mail: yao.s.wang@gmail.com).

Michael K. Ng is with Department of Mathematics, The University of Hong Kong, Pokfulam, Hong Kong (e-mail: mng@maths.hku.hk).

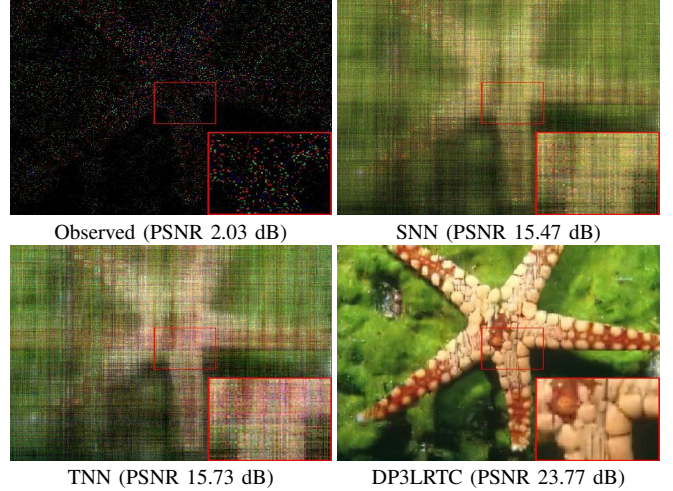


Fig. 1. The recovered results by SNN, TNN, and the proposed DP3LRTC on color image *Starfish* with the sampling rate 5% .

where \mathbf{X} is the underlying matrix, \mathbf{O} is the observed incomplete matrix, Ω is the index set corresponding to the observed entries, and $\mathcal{P}_{\Omega}(\cdot)$ is the projection function that keeps the entries in Ω while setting others be zeros. For gray images, the low-rankness is characterized by the matrix rank or its convex envelope, i.e., the nuclear norm. For multi-dimensional images, the image elements are usually reorder into a matrix, which is known as matricization or unfolding.

However, matricization will inevitably destroy the intrinsic structure of multi-dimensional images. As the higher-order extension of the matrix, the tensor can provide a more natural and compact representation for multi-dimensional images. Thus we can formulate the image completion problem as the following low-rank tensor completion (LRTC) model:

$$\arg \min_{\mathcal{X}} \text{rank}(\mathcal{X}) \quad \text{s.t. } \mathcal{P}_{\Omega}(\mathcal{X}) = \mathcal{P}_{\Omega}(\mathcal{O}), \quad (2)$$

where \mathcal{X} is the underlying tensor and \mathcal{O} is the observed incomplete tensor (as shown in the top-left of Fig. 1). Moreover, we generally considers element-wise sampling in the model (2) and can be extended to the structured sampling, e.g., inpainting [1] and demosaicing [8].

Different from the matrix case, there is not an exact (or unique) definition for tensor rank. Thus, how to define the tensor rank become an important task. Many research efforts have been devoted to this topic [9–12], such as the CAN-DECOMP/PARAFAC (CP) rank and the Tucker rank. The CP rank is defined based on the CP decomposition, where an n -th order tensor is decomposed as the sum of rank-one

tensors, i.e., the outer product of n vectors. The CP rank is defined as the minimal number of the rank-one tensors required to express the target tensor [13]. However, its related optimization is difficult, and even determining the CP rank of a given tensor is NP-hard [14]. The Tucker rank is based on the Tucker decomposition which decomposes a tensor into a core tensor multiplied by a matrix along each mode [15–19]. The Tucker rank is defined as the vector consisting of the ranks of unfolding matrices. The Tucker rank has been considered in the LRTC problem by minimizing its convex surrogate, i.e., the sum of the nuclear norm (SNN) [15]. The top-right of Fig. 1 exhibits the recovered result by the SNN-based model. However, unfolding the tensor along each mode will also destroy the intrinsic structures of the tensor.

The tensor singular value decomposition (t-SVD), based on the tensor-tensor product (t-product), has been emerged as a powerful tool for preserving the intrinsic structures of the tensor [20, 21]. Although the t-SVD is originally suggested for third-order tensors, the t-SVD has been extended to n -th order tensors ($n \geq 3$) [22, 23]. Based on the t-SVD, the corresponding multi-rank and tubal-rank have received considerable attention. The tensor nuclear norm (TNN) [24–27] is suggested as a convex surrogate of the multi-rank. The TNN-based LRTC model is given as follows:

$$\arg \min_{\mathcal{X}} \|\mathcal{X}\|_{\text{TNN}} \quad \text{s.t.} \quad \mathcal{P}_{\Omega}(\mathcal{X}) = \mathcal{P}_{\Omega}(\mathcal{O}), \quad (3)$$

where $\|\mathcal{X}\|_{\text{TNN}} = \sum_{i=1}^{n_3} \|\bar{\mathbf{X}}^{(i)}\|_*$, $\bar{\mathbf{X}}^{(i)}$ is the i -th frontal slice of \mathcal{X} , and $\bar{\mathcal{X}}$ is the tensor generated by performing discrete Fourier transformation (DFT) along the mode-3 fibers (tubes) of \mathcal{X} , i.e., $\bar{\mathcal{X}} = \text{fft}(\mathcal{X}, [], 3)$. The TNN regularizer has the advantage of preserving the global structure of multi-dimensional images. We can observe from Fig. 1 that the recovered result by the TNN-based method (bottom-left) is slightly better than that by the SNN-based method (top-right).

Although utilizing the low-rankness prior has shown its effectiveness for tensor completion, these methods suffer from two drawbacks. First, many real-world multi-dimensional images contain not only global structures but also fine details, which may not be well captured by low-rank regularizer. Second, when the sampling rate is extremely low, the low-rankness itself is not sufficient for the recovery of the underlying tensor. These phenomena can be observed in Fig. 1, where results by the SNN-based model and TNN-based model are of low quality when the sampling rate is 5%.

Therefore, many LRTC methods introduce additional regularizers to introduce image priors. For example, the total variation (TV) regularizer, framelet regularizer, and nonlocal regularizer have received much attention [28–31]. In particular, the TV regularizer was incorporated into the TNN-based model by exploiting the local smoothness [32]. Recently, deep learning-based methods have been developed to learn data-driven priors from a large number of natural images [33–35] and have shown promising performance on extensive application. Therefore, it is reasonable to leverage the power of deep learning-based methods to the LRTC problem.

In this work, we attempt to exploit the respective strengths of the deterministic low-rankness prior and the data-driven deep image prior. By integrating the low-rankness prior with

deep image prior expressed by an implicit regularizer, we suggest the novel LRTC model as follows:

$$\arg \min_{\mathcal{X}} \|\mathcal{X}\|_{\text{TNN}} + \lambda \Phi(\mathcal{X}) \quad \text{s.t.} \quad \mathcal{P}_{\Omega}(\mathcal{X}) = \mathcal{P}_{\Omega}(\mathcal{O}), \quad (4)$$

where $\Phi(\mathcal{X})$ is an implicit regularizer to plug in the denoising neural networks (termed as deep denoisers). In (4), the two regularizers are organically combined and benefit from each other. On the one hand, TNN can capture the global structure, compensating for the denoising neural network deficiency that the receptive field is not able to reach the whole data. On the other hand, the implicit regularizer can bring in deep image priors to compensate the fine details which can hardly be captured by the TNN regularizer. To efficiently solve the proposed model, we develop the alternating direction method of multipliers (ADMM) under the highly flexible Plug-and-Play (PnP) framework, which allows us to plug in the state-of-the-art deep denoisers. We term our method as **deep plug-and-play prior for low-rank tensor completion (DP3LRTC)**. From the bottom-right of Fig. 1, we can observe that the deterministic low-rankness prior and data-driven deep image prior contribute to the superior performance of the proposed DP3LRTC.

The rest of this paper is organized as follows. Section II presents minimal preliminaries necessary for the subsequent discussion. Section III gives the corresponding solving algorithm to tackle the proposed model. Section IV gives the experimental results and discusses details about the DP3LRTC. Section V concludes this paper.

II. PRELIMINARIES

In this section, we introduce minimal and necessary preliminaries of the modular parts, i.e., TNN and PnP, for the subsequent discussion.

A. Notations

In this subsection, we give the basic notations and briefly introduce some definitions. We denote vectors as bold lowercase letters (e.g., \mathbf{x}), matrices as uppercase letters (e.g., \mathbf{X}), and tensors as calligraphic letters (e.g., \mathcal{X}). For a third-order tensor $\mathcal{X} \in \mathbb{R}^{n_1 \times n_2 \times n_3}$, with the MATLAB notation, we denote its (i, j, k) -th element as $\mathcal{X}(i, j, k)$ or $\mathcal{X}_{i,j,k}$. Its (i, j) -th mode-1, mode-2, and mode-3 fibers are denoted as $\mathcal{X}(:, i, j)$, $\mathcal{X}(i, :, j)$, and $\mathcal{X}(i, j, :)$, respectively. We use $\mathcal{X}(i, :, :)$, $\mathcal{X}(:, i, :)$, and $\mathcal{X}(:, :, i)$ to denote the i -th horizontal, lateral, and frontal slices of \mathcal{X} , respectively. More compactly, we also use $\mathbf{X}^{(i)}$ to represent the i -th frontal slices $\mathcal{X}(:, :, i)$. The Frobenius norm of \mathcal{X} is defined as $\|\mathcal{X}\|_F := \sqrt{\sum_{i,j,k} |\mathcal{X}(i, j, k)|^2}$.

B. T-SVD and TNN

For a third-order tensor $\mathcal{X} \in \mathbb{R}^{n_1 \times n_2 \times n_3}$, the block circulation operation [21] is defined as

$$\text{bcirc}(\mathcal{X}) := \begin{pmatrix} \mathbf{X}^{(1)} & \mathbf{X}^{(n_3)} & \dots & \mathbf{X}^{(2)} \\ \mathbf{X}^{(2)} & \mathbf{X}^{(1)} & \dots & \mathbf{X}^{(3)} \\ \vdots & \vdots & \ddots & \vdots \\ \mathbf{X}^{(n_3)} & \mathbf{X}^{(n_3-1)} & \dots & \mathbf{X}^{(1)} \end{pmatrix} \in \mathbb{R}^{n_1 n_3 \times n_2 n_3}.$$

The block diagonalization operation and its inverse operation are defined as

$$\text{bdiag}(\mathcal{X}) := \begin{pmatrix} \mathbf{X}^{(1)} & & & \\ & \mathbf{X}^{(2)} & & \\ & & \ddots & \\ & & & \mathbf{X}^{(n_3)} \end{pmatrix} \in \mathbb{R}^{n_1 n_3 \times n_2 n_3},$$

$$\text{unbdiag}(\text{bdiag}(\mathcal{X})) := \mathcal{X}.$$

The block unfolding operation and its inverse operation are defined as

$$\text{unfold}(\mathcal{X}) := ((\mathbf{X}^{(1)})^T, (\mathbf{X}^{(2)})^T, \dots, (\mathbf{X}^{(n_3)})^T)^T \in \mathbb{R}^{n_1 n_3 \times n_2},$$

$$\text{fold}(\text{unfold}(\mathcal{X})) := \mathcal{X}.$$

Definition 1 (*t-product* [21]): The *t-product*, denoted as “*”, between two third-order tensors $\mathcal{X} \in \mathbb{R}^{n_1 \times n_2 \times n_3}$ and $\mathcal{Y} \in \mathbb{R}^{n_2 \times n_4 \times n_3}$ is defined as

$$\mathcal{Z} = \mathcal{X} * \mathcal{Y} := \text{fold}(\text{bcirc}(\mathcal{X})\text{unfold}(\mathcal{Y})) \in \mathbb{R}^{n_1 \times n_4 \times n_3}.$$

Definition 2 (*special tensors* [21]): The **conjugate transpose** of a third-order tensor $\mathcal{X} \in \mathbb{R}^{n_1 \times n_2 \times n_3}$, denote as \mathcal{X}^H , is the tensor obtained by conjugate transposing each of the frontal slices and then reversing the order of transposed frontal slices 2 through n_3 . The **identity tensor** $\mathcal{I} \in \mathbb{R}^{n_1 \times n_2 \times n_3}$ is the tensor whose first frontal slice is the identity matrix, and other frontal slices are all zeros. A third-order tensor \mathcal{Q} is **orthogonal** if $\mathcal{Q} * \mathcal{Q}^H = \mathcal{Q}^H * \mathcal{Q} = \mathcal{I}$. A third-order tensor \mathcal{S} is **f-diagonal** if each of its frontal slices is a diagonal matrix.

Theorem 1 (*t-SVD* [21]): Let $\mathcal{X} \in \mathbb{R}^{n_1 \times n_2 \times n_3}$ be a third-order tensor, then it can be decomposed as

$$\mathcal{X} = \mathcal{U} * \mathcal{S} * \mathcal{V}^H,$$

where $\mathcal{U} \in \mathbb{R}^{n_1 \times n_1 \times n_3}$ and $\mathcal{V} \in \mathbb{R}^{n_2 \times n_2 \times n_3}$ are the orthogonal tensors, and $\mathcal{S} \in \mathbb{R}^{n_1 \times n_2 \times n_3}$ is a f-diagonal tensor.

The t-SVD can be efficiently obtained by computing a series of matrix SVDs in the Fourier domain; see Algorithm 1 for more details. Based on t-SVD, we have the definitions of the corresponding multi-rank and tubal-rank.

Algorithm 1 The t-SVD for a third-order tensor.

Input: $\mathcal{X} \in \mathbb{R}^{n_1 \times n_2 \times n_3}$.

- 1: $\bar{\mathcal{X}} \leftarrow \text{fft}(\mathcal{X}, [], 3)$.
- 2: **for** $i = 1$ to n_3 **do**
- 3: $[U, S, V] = \text{svd}(\bar{\mathcal{X}}^{(i)})$.
- 4: $\bar{U}^{(i)} \leftarrow U$; $\bar{S}^{(i)} \leftarrow S$; $\bar{V}^{(i)} \leftarrow V$.
- 5: **end for**
- 6: $\mathcal{U} \leftarrow \text{ifft}(\bar{U}, [], 3)$.
- 7: $\mathcal{S} \leftarrow \text{ifft}(\bar{S}, [], 3)$.
- 8: $\mathcal{V} \leftarrow \text{ifft}(\bar{V}, [], 3)$.

Output: $\mathcal{U}, \mathcal{S}, \mathcal{V}$.

Definition 3 (*tensor tubal-rank and multi-rank* [25]): Let $\mathcal{X} \in \mathbb{R}^{n_1 \times n_2 \times n_3}$ be a third-order tensor, the tensor multi-rank, denoted as $\text{rank}_m(\mathcal{X}) \in \mathbb{R}^{n_3}$, is a vector whose i -th element is the rank of i -th frontal slice of \mathcal{X} , where $\bar{\mathcal{X}} = \text{fft}(\mathcal{X}, [], 3)$. The tubal-rank of \mathcal{X} , denote as $\text{rank}_t(\mathcal{X})$, is defined as the

number of non-zero tubes of \mathcal{S} , where \mathcal{S} comes from the t-SVD of \mathcal{X} : $\mathcal{X} = \mathcal{U} * \mathcal{S} * \mathcal{V}^H$. That is, $\text{rank}_t(\mathcal{X}) = \max(\text{rank}_m(\mathcal{X}))$.

Definition 4 (*TNN* [25]): The tensor nuclear norm of a tensor $\mathcal{X} \in \mathbb{R}^{n_1 \times n_2 \times n_3}$, denoted as $\|\mathcal{X}\|_{\text{TNN}}$, is defined as the sum of singular values of all the frontal slices of $\bar{\mathcal{X}}$, i.e.,

$$\|\mathcal{X}\|_{\text{TNN}} := \sum_{i=1}^{n_3} \|\bar{\mathcal{X}}^{(i)}\|_*.$$

where $\bar{\mathcal{X}}^{(i)}$ is the i -th frontal slice of $\bar{\mathcal{X}}$, and $\bar{\mathcal{X}} = \text{fft}(\mathcal{X}, [], 3)$.

C. Plug-and-Play (PnP) Framework

PnP is a highly flexible framework [36–38] that leverages the power of the state-of-the-art denoisers in the ADMM or other proximal algorithms. After variable splitting technique, the optimization problem is decoupled into easier subproblems, one of which is the proximal operator of regularization. The proximal operator of regularization $\text{prox}_{\Phi} : \mathbb{R}^n \rightarrow \mathbb{R}^n$ is defined as

$$\text{prox}_{\Phi}(y) = \arg \min_x \left\{ \Phi(x) + \frac{\rho}{2} \|x - y\|^2 \right\}, \quad (5)$$

which maps the input y to the minimizer of (5). Under the PnP framework, the proximal operator of regularization is replaced by the denoising algorithm (termed as denoiser), which maps the noisy image to the clean image. Here the denoiser serves as an implicit regularizer to express the deep image prior. Regularization by Denoising (RED) [39, 40], which uses the denoising engine in defining the regularization of the inverse problem, is also suggested as an alternative framework.

The state-of-the-art denoisers can be flexibly plugged in as a modular part under the PnP framework. In the past decades, the hand-crafted denoisers, which exploit the deterministic priors of the nature images, have been dominantly used, e.g., TV denoiser [41], framelet denoiser [42], BM3D denoiser [43], WNNM denoiser [44], and ITS denoiser [45]. Recently, deep learning-based denoisers have been rapidly developed to learn data-driven image priors from a large number of natural images [33–35] and have shown promising performance. The PnP framework, which integrates modern denoiser, has shown great empirical success on diverse applications including denoising, tomography, interpolation, super-resolution, and fusion [46–55].

However, even the most basic question of convergence is still a challenging problem. The convergence of the PnP framework has been considered from the fixed-point viewpoint in [38]. Very recently, the convergence of the PnP framework with properly trained denoisers has been considered in [56].

III. THE PROPOSED MODEL AND ALGORITHM

In this section, we develop the ADMM [57, 58] to tackle the minimization problem (4) under the PnP framework. First, we denote the indicator function as

$$1_{\mathbb{S}}(\mathcal{X}) = \begin{cases} 0, & \text{if } \mathcal{X} \in \mathbb{S}, \\ \infty, & \text{otherwise,} \end{cases} \quad (6)$$

where $\mathbb{S} := \{\mathcal{X} \in \mathbb{R}^{n_1 \times n_2 \times n_3}, \mathcal{P}_\Omega(\mathcal{X}) = \mathcal{P}_\Omega(\mathcal{O})\}$ and introduce two auxiliary variables \mathcal{Y} and \mathcal{Z} . Then, we reformulate (4) as a constrained optimization problem, i.e.,

$$\begin{aligned} \arg \min_{\mathcal{X}, \mathcal{Y}, \mathcal{Z}} \quad & \|\mathcal{Y}\|_{\text{TNN}} + \lambda\Phi(\mathcal{Z}) + 1_{\mathbb{S}}(\mathcal{X}) \\ \text{s.t.} \quad & \mathcal{Y} = \mathcal{X}, \mathcal{Z} = \mathcal{X}. \end{aligned} \quad (7)$$

The augmented Lagrangian function of (7) is

$$\begin{aligned} L = & \|\mathcal{Y}\|_{\text{TNN}} + \lambda\Phi(\mathcal{Z}) + 1_{\mathbb{S}}(\mathcal{X}) + \langle \mathcal{X} - \mathcal{Y}, \Lambda_1 \rangle \\ & + \frac{\beta}{2} \|\mathcal{X} - \mathcal{Y}\|_F^2 + \langle \mathcal{X} - \mathcal{Z}, \Lambda_2 \rangle + \frac{\beta}{2} \|\mathcal{X} - \mathcal{Z}\|_F^2, \end{aligned} \quad (8)$$

where Λ_1 and Λ_2 are the Lagrangian multipliers, and β is a nonnegative penalty parameter.

According to the ADMM framework, the solution of (4) can be found by solving a sequence of subproblems.

In **Step 1**, we need to solve the $[\mathcal{Y}, \mathcal{Z}]$ -subproblem. Since the variables \mathcal{Y} and \mathcal{Z} are decoupled, their optimal solutions can be calculated separately.

1) The \mathcal{Y} -subproblem is

$$\arg \min_{\mathcal{Y}} \|\mathcal{Y}\|_{\text{TNN}} + \frac{\beta}{2} \|\mathcal{X}^l - \mathcal{Y} + \Lambda_1^l/\beta\|_F^2. \quad (9)$$

Let the t-SVD of $(\mathcal{X}^l + \Lambda_1^l/\beta)$ be $\mathcal{U} * \mathcal{S} * \mathcal{V}^H$, the closed-form solution of the \mathcal{Y} -subproblem can be exactly calculated via singular value thresholding (SVT) [24, 59, 60] as

$$\mathcal{Y}^{l+1} = \mathcal{U} * \mathcal{D} * \mathcal{V}^H, \quad (10)$$

where \mathcal{D} is an f -diagonal tensor whose each frontal slice in the Fourier domain is $\mathcal{D}(i, i, k) = \max\{\bar{\mathcal{S}}(i, i, k) - \frac{1}{\beta}, 0\}$.

2) The \mathcal{Z} -subproblem is

$$\arg \min_{\mathcal{Z}} \lambda\Phi(\mathcal{Z}) + \frac{\beta}{2} \|\mathcal{X}^l - \mathcal{Z} + \Lambda_2^l/\beta\|_F^2. \quad (11)$$

Let $\sigma = \sqrt{\lambda/\beta}$, then, (11) can be rewritten as

$$\text{prox}_{\Phi}(\mathcal{Z}) = \arg \min_{\mathcal{Z}} \Phi(\mathcal{Z}) + \frac{1}{2\sigma^2} \|\mathcal{Z} - \mathcal{X}^l - \Lambda_2^l/\beta\|_F^2. \quad (12)$$

Under the PnP framework, the proximal operator of regularization $\text{prox}_{\Phi} : \mathbb{R}^{n_1 \times n_2 \times n_3} \rightarrow \mathbb{R}^{n_1 \times n_2 \times n_3}$ is replaced by the deep learning-based denoiser, which maps the noisy image to the clean image. Here we consider the fast and flexible denoising convolutional neural network, namely FFDNet [34], as the deep denoiser. Feeding $\mathcal{X}^l + \Lambda_2^l/\beta$ into the denoiser FFDNet, we obtain the solution of the \mathcal{Z} -subproblem as

$$\mathcal{Z}^{l+1} = \text{FFDNet}(\mathcal{X}^l + \Lambda_2^l/\beta, \sigma). \quad (13)$$

In FFDNet the parameter σ is related to the noise level, but here σ is related to the error level between the estimation and ground truth.

In **Step 2**, we need to solve the \mathcal{X} -subproblem:

$$\begin{aligned} \arg \min_{\mathcal{X}} \quad & 1_{\mathbb{S}}(\mathcal{X}) + \frac{\beta}{2} \|\mathcal{X} - \mathcal{Y}^{l+1} + \Lambda_1^l/\beta\|_F^2 \\ & + \frac{\beta}{2} \|\mathcal{X} - \mathcal{Z}^{l+1} + \Lambda_2^l/\beta\|_F^2. \end{aligned} \quad (14)$$

By minimizing the \mathcal{X} -subproblem, we have $1_{\mathbb{S}}(\mathcal{X}) = 0$, i.e., $\mathcal{X} \in \mathbb{S}$. Thus, the closed-form solution of \mathcal{X} -subproblem is given as follows:

$$\begin{cases} \mathcal{P}_\Omega(\mathcal{X}^{l+1}) = \mathcal{P}_\Omega(\mathcal{O}), \\ \mathcal{P}_{\Omega^c}(\mathcal{X}^{l+1}) = \mathcal{P}_{\Omega^c}\left(\frac{\beta\mathcal{Y}^{l+1} + \beta\mathcal{Z}^{l+1} - \Lambda_1^l - \Lambda_2^l}{2\beta}\right), \end{cases} \quad (15)$$

where Ω^c denotes the complementary set of Ω .

In **Step 3**, we update the multipliers Λ_1 and Λ_2 as follows:

$$\begin{cases} \Lambda_1^{l+1} = \Lambda_1^l + \beta(\mathcal{X}^{l+1} - \mathcal{Y}^{l+1}), \\ \Lambda_2^{l+1} = \Lambda_2^l + \beta(\mathcal{X}^{l+1} - \mathcal{Z}^{l+1}). \end{cases} \quad (16)$$

Finally, the algorithm is summarized in Algorithm 2.

Algorithm 2 The ADMM algorithm for solving (4).

Input: the observed tensor \mathcal{O} , the set index Ω of the observed entries, the parameters β and σ , and the maximum iteration number l_{\max} .

- 1: **Initialization:** the observed tensors \mathcal{Y} , \mathcal{Z} , and \mathcal{X} , the zero tensors Λ_1 and Λ_2 .
- 2: **while** not converged and $l \leq l_{\max}$ **do**
- 3: Updating \mathcal{Y} via (10),
- 4: Updating \mathcal{Z} via (13),
- 5: Updating \mathcal{X} via (15),
- 6: Updating multipliers Λ_1 and Λ_2 via (16).
- 7: **end while**

Output: the recovered tensor \mathcal{X} .

IV. NUMERICAL EXPERIMENTS

In this section, the performance of DP3LRTC will be comprehensively evaluated by experiments on color images, videos, and multi-spectral images (MSIs). Although the FFDNet denoiser is trained for color images, the DP3LRTC can be well generalized for gray videos and MSIs. The DP3LRTC is compared with the baseline methods: SNN [15], TNN [25], and TNN-3DTV [32].

The peak signal to noise ratio (PSNR) and the structural similarity index (SSIM) [61] are chosen as the quality metrics. We report the mean PSNR and mean SSIM of all bands (or frames). The relative change (RelCha) is adopted as the stopping criterion of all methods, which is defined as

$$\text{RelCha} = \frac{\|\mathcal{X}^{l+1} - \mathcal{X}^l\|_F}{\|\mathcal{X}^l\|_F}.$$

In all experiments, when RelCha is smaller than the tolerance 10^{-4} , we stop the iterations. All parameters involved in different methods are manually selected from a candidate set $\{10^{-4}, 10^{-3}, 10^{-2}, 10^{-1}, 1, 10, 10^2\}$ to obtain the highest PSNR value. In this paper, the observed data are elementwisely sampled, except for the color images inpainting and demosaicing.

All the experiments are implemented on Windows 10 and Matlab (R2018a) with an Intel(R) Core(TM) i5-4590 CPU at 3.30 GHz, 16 GB RAM, and NVIDIA GeForce GTX 1060 6GB.

A. Color Image Completion

In this subsection, 8 color images¹ are selected for the color images completion experiments. Each image is rescaled to $[0, 1]$, and the observed elements are element-wisely sampled with different sampling rates. For color images, we use the FFDNet network trained for color images as the PnP denoiser.

Tab. I presents the PSNR and SSIM values of recovered results by different methods. From Tab. I, it can be observed that the TNN-based method obtains better performance than SNN. Since TNN-3DTV introduces additional prior knowledge, it outperforms the TNN-based method and achieves the second best PSNR and SSIM values. The proposed DP3LRTC obtains the highest PSNR and SSIM values. Meanwhile, it is noteworthy that the average margins between the results by DP3LRTC and TNN-3DTV are more than 3.9 dB in PSNR and 0.05 in SSIM.

TABLE I
QUANTITATIVE COMPARISON OF THE RESULTS BY DIFFERENT METHODS ON COLOR IMAGES. THE BEST AND SECOND BEST VALUES ARE HIGHLIGHTED IN BOLD AND UNDERLINED, RESPECTIVELY.

Image	PSNR				SSIM				
	SNN	TNN	TNN-3DTV	DP3LRTC	SNN	TNN	TNN-3DTV	DP3LRTC	
321 × 481 × 3 <i>Starfish</i>	10%	18.48	19.47	<u>22.59</u>	27.43	0.3617	0.3007	<u>0.6345</u>	0.8270
	20%	22.27	22.55	<u>24.85</u>	31.25	0.5476	0.5052	<u>0.7519</u>	0.9143
	30%	24.66	25.71	<u>26.52</u>	34.38	0.6883	0.6685	<u>0.8217</u>	0.9533
512 × 512 × 3 <i>Airplane</i>	10%	20.91	21.94	<u>23.46</u>	28.48	0.6706	0.6623	<u>0.8414</u>	0.9471
	20%	24.81	25.17	<u>25.83</u>	30.57	0.8279	0.8242	<u>0.9220</u>	0.9709
	30%	27.20	27.90	<u>28.45</u>	31.36	0.9060	0.9014	<u>0.9531</u>	0.9806
512 × 512 × 3 <i>Baboon</i>	10%	17.43	17.83	<u>19.56</u>	21.68	0.4077	0.3959	<u>0.5835</u>	0.7798
	20%	19.34	20.07	<u>20.67</u>	23.44	0.5974	0.6005	<u>0.7271</u>	0.8433
	30%	21.17	21.66	<u>21.93</u>	24.06	0.7308	0.7346	<u>0.8083</u>	0.9118
512 × 512 × 3 <i>Fruits</i>	10%	20.73	20.72	<u>24.81</u>	31.47	0.6046	0.5646	<u>0.8363</u>	0.9362
	20%	24.23	24.23	<u>27.31</u>	34.90	0.7777	0.7510	<u>0.9122</u>	0.9621
	30%	26.90	26.99	<u>29.22</u>	36.48	0.8689	0.8541	<u>0.9434</u>	0.9723
512 × 512 × 3 <i>Lena</i>	10%	21.43	21.89	<u>25.96</u>	30.93	0.6415	0.6177	<u>0.8396</u>	0.9241
	20%	24.98	25.68	<u>28.41</u>	32.92	0.8034	0.7888	<u>0.9069</u>	0.9423
	30%	27.71	28.06	<u>30.07</u>	33.46	0.8844	0.8719	<u>0.9380</u>	0.9575
768 × 1024 × 3 <i>Watch</i>	10%	22.47	23.01	<u>26.27</u>	33.96	0.7128	0.7490	<u>0.8863</u>	0.9825
	20%	25.64	26.61	<u>28.46</u>	38.18	0.8641	0.8923	<u>0.9466</u>	0.9888
	30%	28.37	29.70	<u>30.31</u>	40.89	0.9332	0.9502	<u>0.9709</u>	0.9971
586 × 695 × 3 <i>Opera</i>	10%	24.23	25.05	<u>25.56</u>	30.51	0.7499	0.7486	<u>0.8075</u>	0.9300
	20%	27.55	28.24	<u>29.13</u>	33.57	0.8649	0.8734	<u>0.9132</u>	0.9628
	30%	29.80	30.89	<u>31.14</u>	35.90	0.9188	0.9323	<u>0.9447</u>	0.9812
768 × 1024 × 3 <i>Water</i>	10%	20.20	21.00	<u>22.57</u>	26.17	0.5860	0.6126	<u>0.7756</u>	0.9223
	20%	22.75	23.37	<u>24.29</u>	28.74	0.7790	0.6685	<u>0.8822</u>	0.9472
	30%	24.67	25.76	<u>25.88</u>	30.65	0.8767	0.8922	<u>0.9302</u>	0.9806
Average	10%	20.74	21.36	<u>23.85</u>	28.83	0.5919	0.5814	<u>0.7756</u>	0.9061
	20%	23.95	24.49	<u>26.12</u>	31.70	0.7578	0.7380	<u>0.8703</u>	0.9415
	30%	26.31	27.08	<u>27.94</u>	33.40	0.8509	0.8507	<u>0.9138</u>	0.9668

For visualization, we exhibit the recovered images with the sampling rate 30% in Fig. 2. From the images illustrated in Fig. 2, we can find that the SNN-based method and TNN-based method are able to recover the general structure of the color images, while the details are unclear and results remain artifacts, which can be seen in the enlarged red boxes. The results by TNN-3DTV are relatively better. However, we can observe the over-smoothed phenomena in the enlarged areas. The recovered results by the proposed method are of high quality, being highly clear and very similar to the original images.

Now, we consider the structured samplings, i.e., inpainting and demosaicing, which are more difficult than the element-

wise sampling. In image inpainting and demosaicing, we consider the tubal sampling (i.e., entries are sampled along all channels for a spatial location) and the Bayer pattern sampling (i.e., each two-by-two cell contains two green, one blue, and one red), respectively. In inpainting, there are three different kinds of masks: letters, graffiti, and grid, respectively. Fig. 3 shows the inpainting and demosaicing results by different methods on color images: *Fruits*, *Lena*, *Sailboat*, and *Baboon*. It is easy to observe that the proposed method is superior to competing methods in inpainting and demosaicing experiments.

B. Video Completion

In this subsection, 5 gray videos² with different sizes are selected. For gray videos, we use the FFDNet network trained for gray images as the PnP denoiser. Here we feed the unfolding of $\mathcal{X}^l + \Lambda_2^l/\beta$ into the FFDNet denoiser. Tab. II lists the PSNR and SSIM values of the recovered video results by different methods with different sampling rates. It is easy to observe that DP3LRTC obtains the results with the highest performance evaluation indices. For visualization, we show the 20-th frame of the recovered videos with the sampling rate 20% in Fig. 4. We can see that the results recovered by DP3LRTC are of higher quality than the results obtained by compared methods.

TABLE II
QUANTITATIVE COMPARISONS OF THE RESULTS BY DIFFERENT METHODS ON VIDEOS. THE BEST AND SECOND BEST VALUES ARE HIGHLIGHTED IN BOLD AND UNDERLINED, RESPECTIVELY.

Video	PSNR				SSIM				
	SNN	TNN	TNN-3DTV	DP3LRTC	SNN	TNN	TNN-3DTV	DP3LRTC	
144 × 176 × 30 <i>Akiyo</i>	5%	20.18	28.33	<u>28.76</u>	30.59	0.5976	0.8630	<u>0.8949</u>	0.9294
	10%	23.64	31.16	<u>31.97</u>	33.33	0.7340	0.9272	<u>0.9452</u>	0.9623
	20%	27.54	34.82	<u>36.06</u>	36.96	0.8642	0.9674	<u>0.9777</u>	0.9816
144 × 176 × 30 <i>Suzie</i>	5%	20.84	26.37	<u>27.39</u>	29.37	0.5944	0.7203	<u>0.7989</u>	0.8373
	10%	24.40	28.41	<u>29.27</u>	31.80	0.7046	0.7976	<u>0.8513</u>	0.8899
	20%	28.12	31.14	<u>31.95</u>	34.75	0.8189	0.8739	<u>0.9123</u>	0.9358
144 × 176 × 30 <i>Container</i>	5%	19.81	26.27	<u>26.63</u>	26.87	0.6446	0.8305	<u>0.8611</u>	0.8695
	10%	22.26	29.53	<u>30.05</u>	30.44	0.7413	0.9023	<u>0.9272</u>	0.9230
	20%	25.56	33.65	<u>34.69</u>	34.82	0.8495	0.9553	<u>0.9677</u>	0.9654
144 × 176 × 30 <i>News</i>	5%	18.34	26.65	<u>27.20</u>	28.29	0.5610	0.8182	<u>0.8738</u>	0.9023
	10%	21.47	30.31	<u>30.56</u>	31.96	0.6955	0.9106	<u>0.9285</u>	0.9473
	20%	25.00	33.82	<u>34.21</u>	35.55	0.8256	0.9554	<u>0.9665</u>	0.9740
256 × 256 × 30 <i>Bus</i>	5%	15.79	18.30	<u>18.36</u>	20.78	0.3300	0.3331	<u>0.3973</u>	0.5932
	10%	17.70	19.61	<u>19.66</u>	22.83	0.4174	0.4421	<u>0.5083</u>	0.7222
	20%	19.86	21.74	<u>21.91</u>	25.48	0.5560	0.5993	<u>0.6778</u>	0.8359
Average	5%	18.99	25.18	<u>25.67</u>	27.18	0.5455	0.7130	<u>0.7652</u>	0.8263
	10%	21.89	27.80	<u>28.30</u>	30.07	0.6586	0.7960	<u>0.8321</u>	0.8889
	20%	25.22	31.03	<u>31.76</u>	33.51	0.7828	0.8703	<u>0.9004</u>	0.9385

C. MSI Completion

In this subsection, we test 7 MSIs from the *CAVE* dataset³ which are of size $256 \times 256 \times 31$ with the wavelengths in the range of 400 ~ 700 nm at an interval of 10 nm. For MSIs, we use the FFDNet network trained for gray images as the PnP denoiser. Here we feed the unfolding of $\mathcal{X}^l + \Lambda_2^l/\beta$ into FFDNet denoiser.

²Available at <http://trace.eas.asu.edu/yuv/>.

³Available at <http://www.cs.columbia.edu/CAVE/databases/multispectral/>.

¹Available at <http://sipi.usc.edu/database/database.php>.

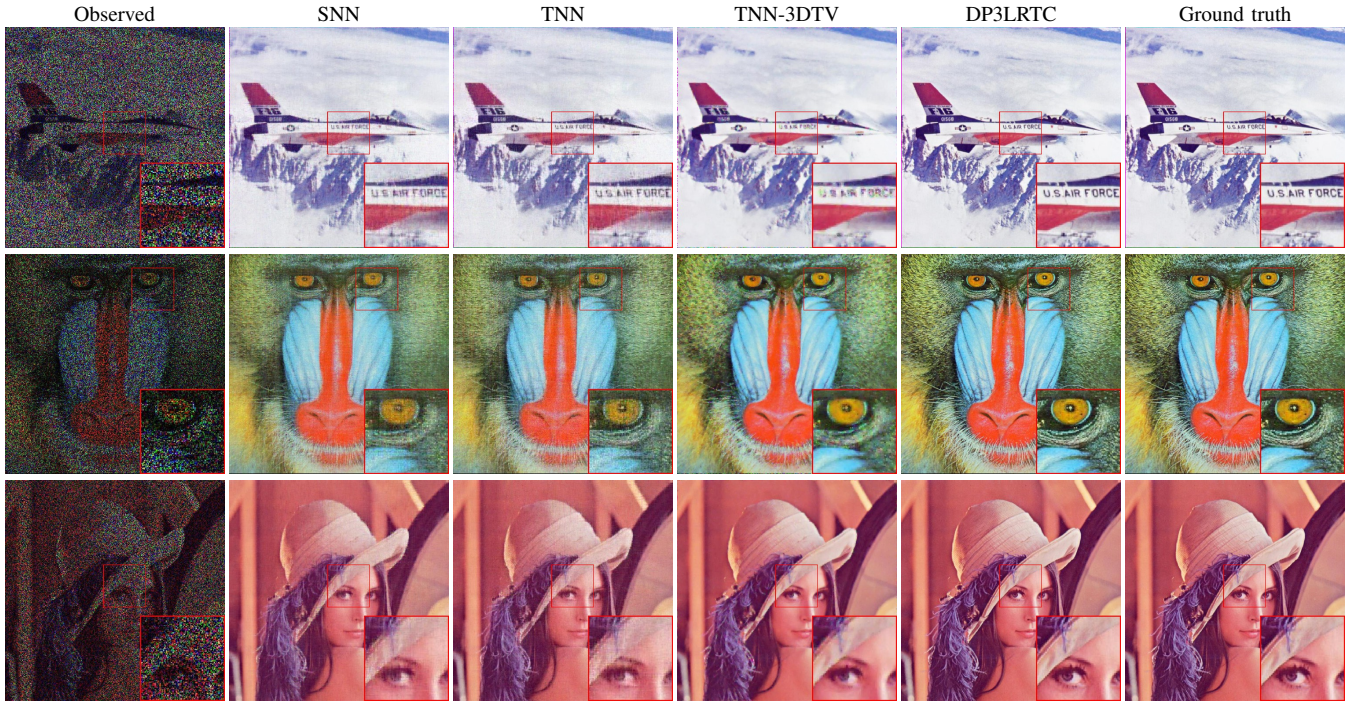


Fig. 2. The recovered color images by SNN, TNN, TNN-3DTV, and DP3LRTC with the sampling rate 30%.

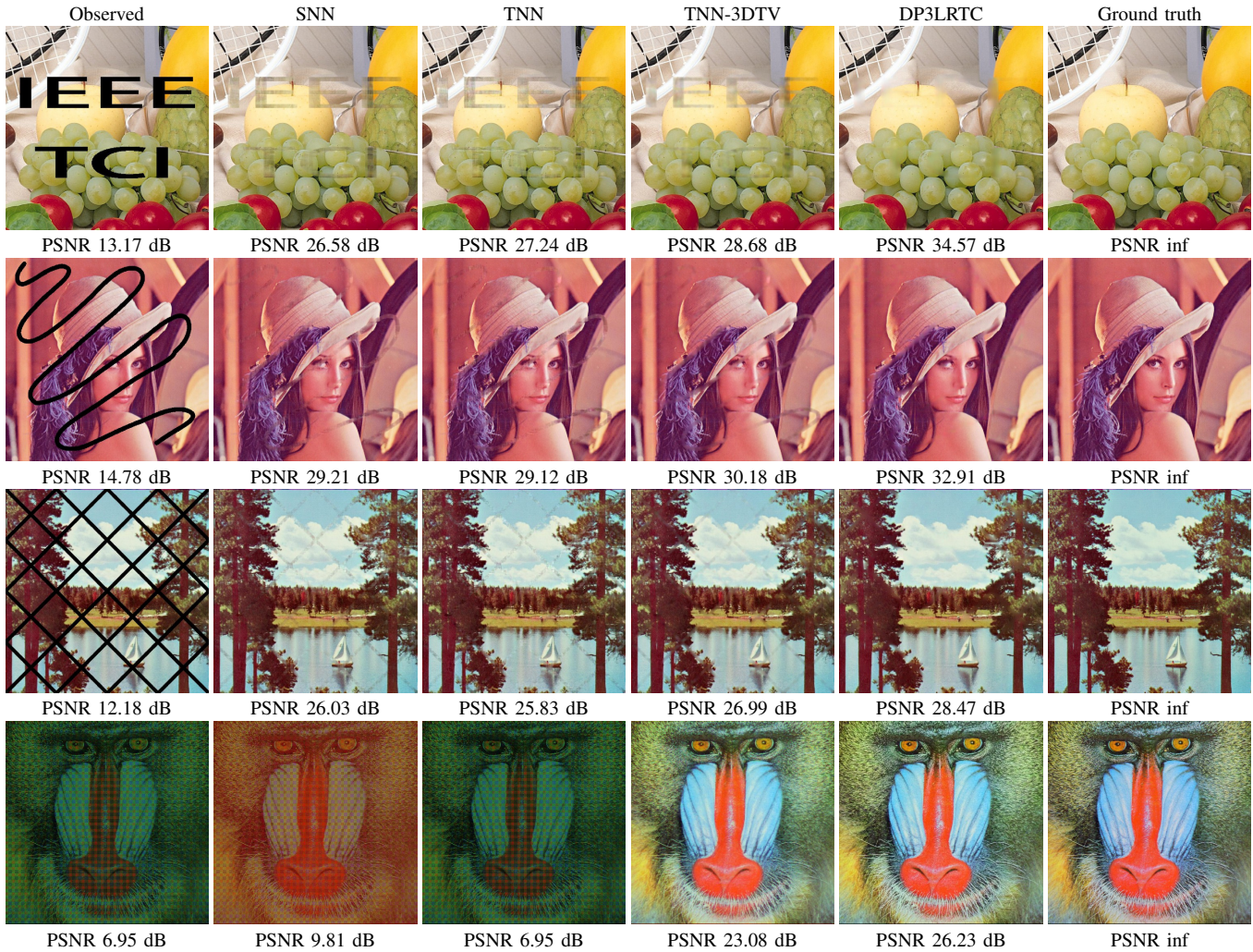


Fig. 3. Inpainting (top three rows) and demosaicing (bottom row) results by SNN, TNN, TNN-3DTV, and DP3LRTC on color images.

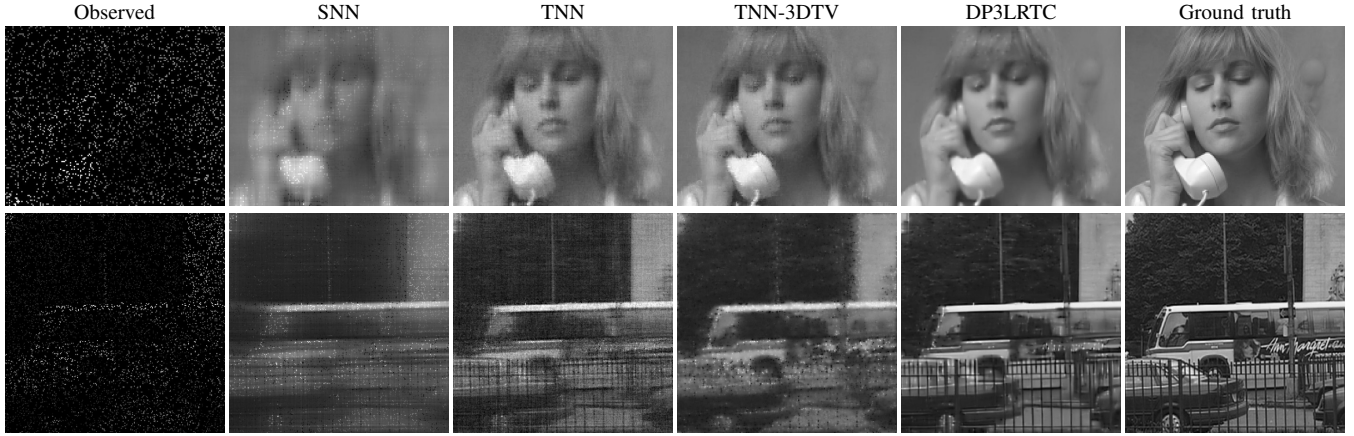


Fig. 4. The 20-th frame of the videos recovered by SNN, TNN, TNN-3DTV, and DP3LRTC with the sampling rate 10%.

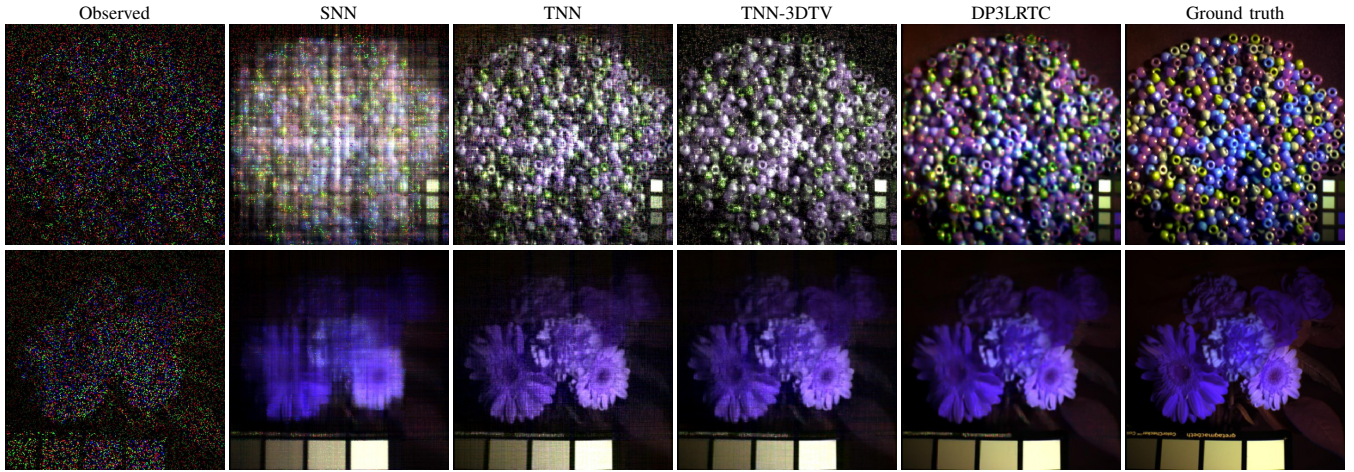


Fig. 5. The MSIs (pseudo-color images composed of the 1st, 2nd, and 31-st bands) recovered by SNN, TNN, TNN-3DTV, and DP3LRTC with the sampling rate 10%.

TABLE III
QUANTITATIVE COMPARISON OF THE RESULTS BY DIFFERENT METHODS ON MSIS. THE **BEST** AND SECOND BEST VALUES ARE HIGHLIGHTED IN BOLD AND UNDERLINED, RESPECTIVELY.

MSI		PSNR				SSIM			
		SNN	TNN	TNN-3DTV	DP3LRTC	SNN	TNN	TNN-3DTV	DP3LRTC
<i>Balloons</i>	5%	24.29	31.35	<u>32.66</u>	39.04	0.8232	0.8670	<u>0.9381</u>	0.9843
	10%	31.27	35.63	<u>37.66</u>	42.98	0.9242	0.9380	<u>0.9735</u>	0.9937
	20%	37.34	41.11	<u>42.77</u>	47.54	0.9737	0.9803	<u>0.9904</u>	0.9975
<i>Beads</i>	5%	16.50	19.86	<u>21.27</u>	22.53	0.3259	0.4569	<u>0.6506</u>	0.6912
	10%	17.99	22.92	<u>23.95</u>	26.08	0.4191	0.6512	<u>0.7907</u>	0.8369
	20%	21.34	27.61	<u>27.78</u>	30.20	0.6404	0.8420	<u>0.9024</u>	0.9319
<i>Cd</i>	5%	22.19	26.51	<u>29.35</u>	30.22	0.8497	0.8029	<u>0.9251</u>	0.9597
	10%	25.98	29.54	<u>31.92</u>	35.30	0.9018	0.8871	<u>0.9550</u>	0.9790
	20%	30.85	33.22	<u>36.04</u>	39.35	0.9498	0.9447	<u>0.9791</u>	0.9890
<i>Clay</i>	5%	28.83	33.62	<u>34.25</u>	39.89	0.9224	0.9052	<u>0.9487</u>	0.9680
	10%	35.78	38.22	<u>39.66</u>	43.80	0.9726	0.9657	<u>0.9819</u>	0.9907
	20%	41.58	43.69	<u>44.69</u>	48.02	0.9895	0.9813	<u>0.9890</u>	0.9952
<i>Face</i>	5%	25.64	32.32	<u>32.70</u>	36.82	0.8346	0.8981	<u>0.9381</u>	0.9663
	10%	30.51	36.50	<u>37.52</u>	39.66	0.9125	0.9548	<u>0.9736</u>	0.9829
	20%	36.20	41.33	<u>42.00</u>	42.96	0.9664	0.9842	<u>0.9778</u>	0.9916
<i>Feathers</i>	5%	20.45	27.55	<u>28.23</u>	31.14	0.6565	0.7694	<u>0.8712</u>	0.9375
	10%	24.88	30.36	<u>31.83</u>	34.59	0.7925	0.8717	<u>0.9308</u>	0.9656
	20%	29.30	35.86	<u>36.73</u>	38.68	0.8995	0.9481	<u>0.9726</u>	0.9838
<i>Flowers</i>	5%	20.47	26.75	<u>27.90</u>	30.34	0.6293	0.7153	<u>0.8288</u>	0.8894
	10%	27.28	32.05	<u>33.42</u>	37.70	0.7605	0.8357	<u>0.9025</u>	0.9419
	20%	29.49	35.33	<u>36.25</u>	37.66	0.8804	0.9342	<u>0.9621</u>	0.9745
Average	5%	22.62	28.28	<u>29.48</u>	32.85	0.7202	0.7735	<u>0.8715</u>	0.9138
	10%	27.28	32.05	<u>33.42</u>	36.59	0.8119	0.8720	<u>0.9297</u>	0.9558
	20%	32.30	36.88	<u>38.04</u>	40.63	0.9000	0.9450	<u>0.9676</u>	0.9805

Tab. III exhibits the PSNR and SSIM values of all the results by different methods. The DP3LRTC achieves the highest PSNR and SSIM values, while the TNN-3DTV gets the second best. Fig. 5 displays the recovered MSIs (pseudo-color images composed of the 1st, 2nd, and 31-st bands) by different methods with the sampling rate 10%. From Fig. 5, it can be observed that the results recovered by DP3LRTC are of the highest quality. In Fig. 6, we display one selected tube of results recovered by SNN, TNN, TNN-3DTV, and DP3LRTC on MSI *Balloons* with the sampling rate 10%. We can observe that the selected tube of the MSI recovered by DP3LRTC is closer to the ground truth as compared with those by SNN, TNN, and TNN-3DTV.

D. Discussions

1) *Convergence*: The numerical experiments have shown the great empirical success of DP3LRTC. However, it is still an open question whether the ADMM algorithm under the PnP framework has a good convergence behavior. In Fig. 7, we displayed the relative change curves of the ADMM algorithm (in the logarithmic scale) with respect to the iteration on different videos. We can evidently observe the numerical convergence of the ADMM algorithm.

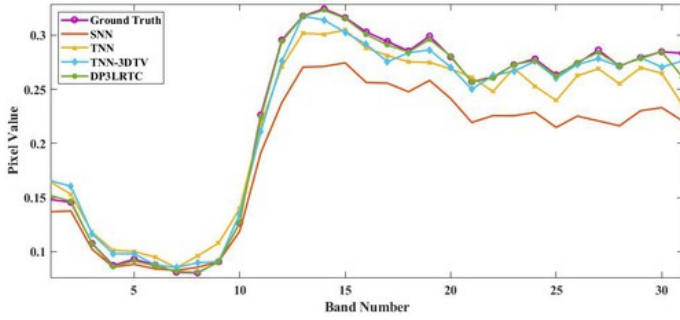


Fig. 6. The selected tubes of results recovered by SNN, TNN, TNN-3DTV, and DP3LRTC on MSIs *Balloons* with the sampling rate 10%.

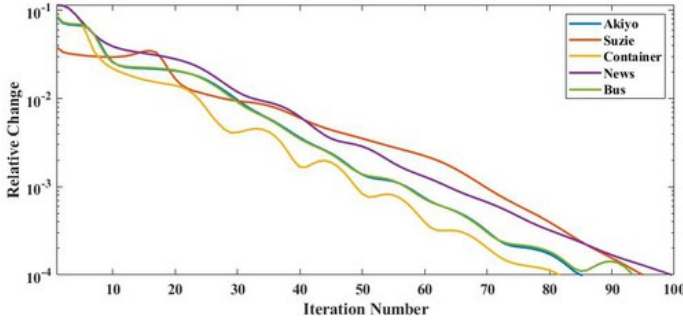


Fig. 7. The convergence curves of the ADMM algorithm on videos *Akiyo*, *Suzie*, *Container*, *News*, and *Bus* with the sampling rate 10%.

2) *Parameter Analysis*: In this subsection, we analyze the effect of parameters β and σ . In Fig. 8, we show the PSNR and SSIM values of the results recovered by DP3LRTC on color image *Starfish* with respect to β and σ . We can see that DP3LRTC delivers the best performance when $\beta \in \{10^{-1}, 1\}$ and $\sigma \in \{10^{-2}, 10^{-1}, 1\}$.

3) *Contributions of Different Terms*: To evaluate the contributions of the low-rankness prior and deep image prior, we test the performance of 3 methods: TNN (only the TNN regularizer), DPR (only the implicit deep regularizer), and DP3LRTC (both the TNN and implicit deep regularizers). In Fig. 9, we exhibit the recovered results by TNN, DPR, and DP3LRTC on color image *Airplane* and MSI *Flowers*, together with PSNR values. We can observe from Fig. 9 that the performance of DPR is comparable to DP3LRTC on color images, while DP3LRTC largely outperforms DPR on MSIs due to the spectral redundancy of MSIs. Therefore, we can confirm from that two regularizers are indispensable to DP3LRTC and benefit from each other. Together, they contribute the superior performance of the proposed DP3LRTC.

4) *Beyond Third-order Tensors*: In order to demonstrate that DP3LRTC can be extended to high-order tensors ($n \geq 3$), we have conducted the experiment on the fourth-order tensor i.e., color video “*Suzie*”⁴ of size $144 \times 176 \times 3 \times 100$. Here we adopt the extension of TNN for high-order tensors [23]. For color videos, we use the FFDNet network trained for color images as the PnP denoiser. Each frame of the color video is denoised as a color image. We reported the quantitative comparison of the recovered results by SNN, TNN, and DP3LRTC on

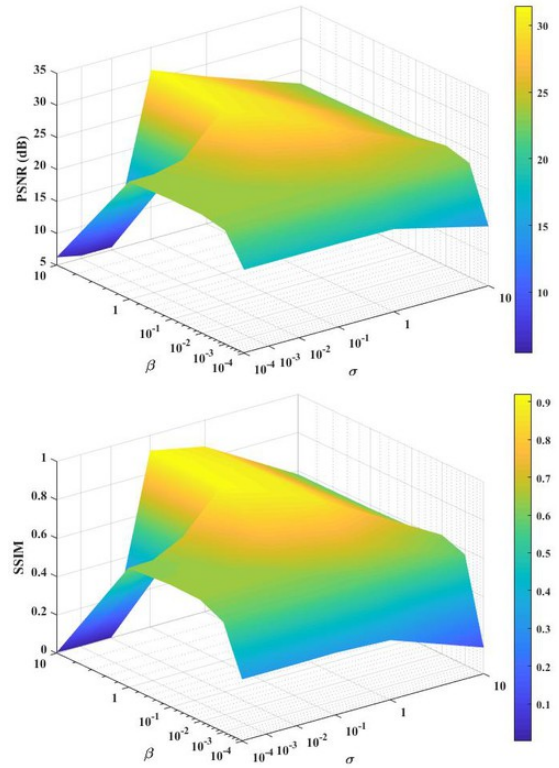


Fig. 8. The PSNR and SSIM values of the results recovered by DP3LRTC with respect to β and σ on color image *Starfish* with the sampling rate 20%.

color video *Suzie* in Tab. IV. For better visual inspection, we further displayed the recovered results by SNN, TNN, and DP3LRTC in Fig. 10. We can observe that DP3LRTC can be easily extended to handle high-order tensors.

TABLE IV
QUANTITATIVE COMPARISON OF THE RESULTS BY DIFFERENT METHODS ON COLOR VIDEO. THE BEST ARE HIGHLIGHTED IN BOLD.

Color Video	PSNR			SSIM		
	SNN	TNN	DP3LRTC	SNN	TNN	DP3LRTC
1%	7.44	23.26	24.96	0.0372	0.6967	0.7371
Suzie 5%	17.97	28.24	30.73	0.5148	0.8384	0.8891
10%	21.22	30.94	33.47	0.6139	0.8943	0.9285

V. CONCLUSIONS

In this paper, we proposed a hybrid tensor completion model, in which the TNN regularizer is utilized to catch the global information and a data-driven implicit regularizer is used to express the local information. The proposed model simultaneously combines the model-based optimization method with the CNN-based method, in consideration of the global structure and fine detail preservation. An efficient ADMM is developed to solve the proposed model. Numerical experiments on different types of multi-dimensional images illustrate the superiority of the proposed method on the tensor completion problem.

REFERENCES

- [1] L. Zhuang and J. M. Bioucas-Dias, “Fast hyperspectral image denoising and inpainting based on low-rank and sparse representations,” *IEEE*

⁴Available at <http://trace.eas.asu.edu/yuv/>

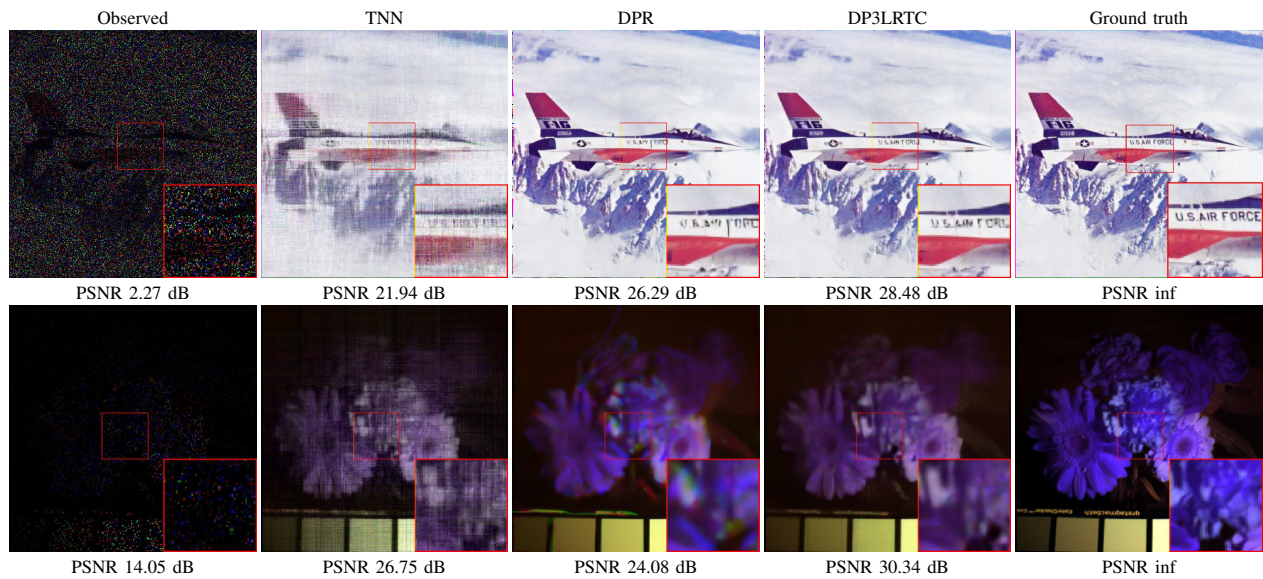


Fig. 9. First row: the recovered results by TNN, DPR, and DP3LRTC on color image *Airplane* with the sampling rate 10%. Second row: the recovered results (pseudo-color images composed of the 1st, 2nd, and 31-th bands) by TNN, DPR, and DP3LRTC on MSI *Flowers* with the sampling rate 5%.



Fig. 10. The 50-th frame of the recovered color video *Suzie* by SNN, TNN, and DP3LRTC with the sampling rate 5%.

- Journal of Selected Topics in Applied Earth Observations and Remote Sensing*, vol. 11, no. 3, pp. 730–742, 2018.
- [2] É. Monier, T. Oberlin, N. Brun, M. Tencé, M. de Frutos, and N. Dobigeon, “Reconstruction of partially sampled multiband images application to STEM-EELS imaging,” *IEEE Transactions on Computational Imaging*, vol. 4, no. 4, pp. 585–598, 2018.
 - [3] Y. Wang, J. Peng, Q. Zhao, Y. Leung, X.-L. Zhao, and D. Meng, “Hyperspectral image restoration via total variation regularized low-rank tensor decomposition,” *IEEE Journal of Selected Topics in Applied Earth Observations and Remote Sensing*, vol. 11, no. 4, pp. 1227–1243, 2018.
 - [4] Y. Chang, L. Yan, H. Fang, and C. Luo, “Anisotropic spectral-spatial total variation model for multispectral remote sensing image destriping,” *IEEE Transactions on Image Processing*, vol. 24, no. 6, pp. 1852–1866, 2015.
 - [5] W.-H. Xu, X.-L. Zhao, T.-Y. Ji, J.-Q. Miao, T.-H. Ma, S. Wang, and T.-Z. Huang, “Laplace function based nonconvex surrogate for low-rank tensor completion,” *Signal Processing: Image Communication*, vol. 73, pp. 62–69, 2019.
 - [6] J.-H. Yang, X.-L. Zhao, T.-H. Ma, Y. Chen, T.-Z. Huang, and M. Ding, “Remote sensing images destriping using unidirectional hybrid total variation and nonconvex low-rank regularization,” *Journal of Computational and Applied Mathematics*, vol. 363, pp. 124–144, 2020.
 - [7] Q. Zhao, D. Meng, X. Kong, Q. Xie, W. Cao, Y. Wang, and Z. Xu, “A novel sparsity measure for tensor recovery,” in *Proceedings of the IEEE International Conference on Computer Vision*, 2015, pp. 271–279.
 - [8] L. Zhuang and J. M. Bioucas-Dias, “Hy-Demosaicing: Hyperspectral blind reconstruction from spectral subsampling,” in *Proceedings of the IEEE International Geoscience and Remote Sensing Symposium*, 2018, pp. 4015–4018.
 - [9] T. G. Kolda and B. W. Bader, “Tensor decompositions and applications,” *SIAM Review*, vol. 51, no. 3, pp. 455–500, 2009.
 - [10] Y. Wang, D. Meng, and M. Yuan, “Sparse recovery: from vectors to tensors,” *National Science Review*, vol. 5, no. 5, pp. 756–767, 2017.
 - [11] Z. Long, Y. Liu, L. Chen, and C. Zhu, “Low rank tensor completion for multiway visual data,” *Signal Processing*, vol. 155, pp. 301–316, 2019.
 - [12] N. D. Sidiropoulos, L. De Lathauwer, X. Fu, K. Huang, E. E. Papalexakis, and C. Faloutsos, “Tensor decomposition for signal processing and machine learning,” *IEEE Transactions on Signal Processing*, vol. 65, no. 13, pp. 3551–3582, 2017.
 - [13] Q. Zhao, L. Zhang, and A. Cichocki, “Bayesian CP factorization of incomplete tensors with automatic rank determination,” *IEEE Transactions on Pattern Analysis and Machine Intelligence*, vol. 37, no. 9, pp. 1751–1763, 2015.
 - [14] C. J. Hillar and L.-H. Lim, “Most tensor problems are NP-hard,” *Journal of the ACM*, vol. 60, no. 6, pp. 1–39, 2013.
 - [15] J. Liu, P. Musialski, P. Wonka, and J. Ye, “Tensor completion for estimating missing values in visual data,” *IEEE Transactions on Pattern Analysis and Machine Intelligence*, vol. 35, no. 1, pp. 208–220, 2013.
 - [16] S. Gandy, B. Recht, and I. Yamada, “Tensor completion and low-n-rank tensor recovery via convex optimization,” *Inverse Problems*, vol. 27, no. 2, p. 025010, 2011.
 - [17] Y. Xu, R. Hao, W. Yin, and Z. Su, “Parallel matrix factorization for low-rank tensor completion,” *Inverse Problems and Imaging*, vol. 9, no. 2, pp. 601–624, 2015.
 - [18] T.-Y. Ji, T.-Z. Huang, X.-L. Zhao, T.-H. Ma, and L.-J. Deng, “A non-convex tensor rank approximation for tensor completion,” *Applied Mathematical Modelling*, vol. 48, pp. 410–422, 2017.
 - [19] Q. Xie, Q. Zhao, D. Meng, and Z. Xu, “Kronecker-basis-representation based tensor sparsity and its applications to tensor recovery,” *IEEE Transactions on Pattern Analysis and Machine Intelligence*, vol. 40, no. 8, pp. 1888–1902, 2018.
 - [20] M. E. Kilmer and C. D. Martin, “Factorization strategies for third-order tensors,” *Linear Algebra and its Applications*, vol. 435, no. 3, pp. 641–658, 2011.
 - [21] M. E. Kilmer, K. Braman, N. Hao, and R. C. Hoover, “Third-order tensors as operators on matrices: A theoretical and computational framework with applications in imaging,” *SIAM Journal on Matrix Analysis and Applications*, vol. 34, no. 1, pp. 148–172, 2013.
 - [22] C. D. Martin, R. Shafer, and B. LaRue, “An order- p tensor factorization with applications in imaging,” *SIAM Journal on Scientific Computing*,

- vol. 35, no. 1, pp. A474–A490, 2013.
- [23] Y.-B. Zheng, T.-Z. Huang, X.-L. Zhao, T.-X. Jiang, T.-Y. Ji, and T.-H. Ma, “Tensor n-tubal rank and its convex relaxation for low-rank tensor recovery,” *arXiv preprint arXiv:1812.00688*, 2018.
- [24] O. Semerci, N. Hao, M. E. Kilmer, and E. L. Miller, “Tensor-based formulation and nuclear norm regularization for multienergy computed tomography,” *IEEE Transactions on Image Processing*, vol. 23, no. 4, pp. 1678–1693, 2014.
- [25] Z.-M. Zhang, G. Ely, S. Aeron, N. Hao, and M. Kilmer, “Novel methods for multilinear data completion and de-noising based on tensor-svd,” in *Proceedings of the IEEE Conference on Computer Vision and Pattern Recognition*, 2014, pp. 3842–3849.
- [26] Z. Zhang and S. Aeron, “Exact tensor completion using t-SVD,” *IEEE Transactions on Signal Processing*, vol. 65, pp. 1511–1526, 2017.
- [27] C. Lu, J. Feng, Y. Chen, W. Liu, Z. Lin, and S. Yan, “Tensor robust principal component analysis: Exact recovery of corrupted low-rank tensors via convex optimization,” in *Proceedings of the IEEE Conference on Computer Vision and Pattern Recognition*, 2016, pp. 5249–5257.
- [28] X.-T. Li, Y. Ye, and X. Xu, “Low-rank tensor completion with total variation for visual data inpainting,” in *Proceedings of the AAAI Conference on Artificial Intelligence*, 2017, pp. 2210–2216.
- [29] Y.-B. Zheng, T.-Z. Huang, T.-Y. Ji, X.-L. Zhao, T.-X. Jiang, and T.-H. Ma, “Low-rank tensor completion via smooth matrix factorization,” *Applied Mathematical Modelling*, vol. 70, pp. 677–695, 2019.
- [30] X.-T. Li, X.-L. Zhao, T.-X. Jiang, Y.-B. Zheng, T.-Y. Ji, and T.-Z. Huang, “Low-rank tensor completion via combined non-local self-similarity and low-rank regularization,” *Neurocomputing*, 2019, doi:10.1016/j.neucom.2019.07.092.
- [31] T.-X. Jiang, T.-Z. Huang, X.-L. Zhao, T.-Y. Ji, and L.-J. Deng, “Matrix factorization for low-rank tensor completion using framelet prior,” *Information Sciences*, vol. 436, pp. 403–417, 2018.
- [32] F. Jiang, X.-Y. Liu, H. Lu, and R. Shen, “Anisotropic total variation regularized low-rank tensor completion based on tensor nuclear norm for color image inpainting,” in *Proceedings of the IEEE International Conference on Acoustics, Speech and Signal Processing*, 2018, pp. 1363–1367.
- [33] K. Zhang, W. Zuo, Y. Chen, D. Meng, and L. Zhang, “Beyond a Gaussian denoiser: Residual learning of deep CNN for image denoising,” *IEEE Transactions on Image Processing*, vol. 26, no. 7, pp. 3142–3155, 2017.
- [34] K. Zhang, W. Zuo, and L. Zhang, “FFDNet: Toward a fast and flexible solution for CNN-based image denoising,” *IEEE Transactions on Image Processing*, vol. 27, no. 9, pp. 4608–4622, 2018.
- [35] L. Zhang and W. Zuo, “Image restoration: from sparse and low-rank priors to deep priors,” *IEEE Signal Processing Magazine*, vol. 34, no. 5, pp. 172–179, 2017.
- [36] S. Sreehari, S. V. Venkatakrishnan, B. Wohlberg, G. T. Buzzard, L. F. Drummy, J. P. Simmons, and C. A. Bouman, “Plug-and-play priors for bright field electron tomography and sparse interpolation,” *IEEE Transactions on Computational Imaging*, vol. 2, no. 4, pp. 408–423, 2016.
- [37] S. V. Venkatakrishnan, C. A. Bouman, and B. Wohlberg, “Plug-and-play priors for model based reconstruction,” in *Proceedings of the IEEE Global Conference on Signal and Information Processing*, 2013, pp. 945–948.
- [38] S. H. Chan, X. Wang, and O. A. Elgendy, “Plug-and-play ADMM for image restoration: Fixed-point convergence and applications,” *IEEE Transactions on Computational Imaging*, vol. 3, no. 1, pp. 84–98, 2016.
- [39] Y. Romano, M. Elad, and P. Milanfar, “The little engine that could: Regularization by denoising (RED),” *SIAM Journal on Imaging Sciences*, vol. 10, no. 4, pp. 1804–1844, 2017.
- [40] E. T. Reehorst and P. Schmitter, “Regularization by denoising: Clarifications and new interpretations,” *IEEE Transactions on Computational Imaging*, vol. 5, no. 1, pp. 52–67, 2018.
- [41] L. I. Rudin, S. Osher, and E. Fatemi, “Nonlinear total variation based noise removal algorithms,” *Physica D: nonlinear phenomena*, vol. 60, no. 1–4, pp. 259–268, 1992.
- [42] J.-F. Cai, B. Dong, S. Osher, and Z. Shen, “Image restoration: total variation, wavelet frames, and beyond,” *Journal of the American Mathematical Society*, vol. 25, no. 4, pp. 1033–1089, 2012.
- [43] K. Dabov, A. Foi, and K. Egiazarian, “Image denoising by sparse 3d transform-domain collaborative filtering,” in *Proceedings of the 15th European Signal Processing Conference*, 2007, pp. 145–149.
- [44] S. Gu, L. Zhang, W. Zuo, and X. Feng, “Weighted nuclear norm minimization with application to image denoising,” in *Proceedings of the IEEE Conference on Computer Vision and Pattern Recognition*, 2014, pp. 2862–2869.
- [45] Q. Xie, Q. Zhao, D. Meng, Z. Xu, S. Gu, W. Zuo, and L. Zhang, “Multispectral images denoising by intrinsic tensor sparsity regularization,” in *Proceedings of IEEE Conference on Computer Vision and Pattern Recognition*, 2016, pp. 1692–1700.
- [46] S. Sreehari, S. Venkatakrishnan, K. L. Bouman, J. P. Simmons, L. F. Drummy, and C. A. Bouman, “Multi-resolution data fusion for super-resolution electron microscopy,” in *Proceedings of the IEEE Conference on Computer Vision and Pattern Recognition Workshops*, 2017, pp. 88–96.
- [47] G. T. Buzzard, S. H. Chan, S. Sreehari, and C. A. Bouman, “Plug-and-play unplugged: Optimization-free reconstruction using consensus equilibrium,” *SIAM Journal on Imaging Sciences*, vol. 11, no. 3, pp. 2001–2020, 2018.
- [48] Y. He, Q. Yao, C. Li, N. Yokoya, and Q. Zhao, “Non-local meets global: An integrated paradigm for hyperspectral denoising,” in *Proceedings of the IEEE Conference on Computer Vision and Pattern Recognition*, 2019.
- [49] Y. Sun, B. Wohlberg, and U. S. Kamilov, “An online plug-and-play algorithm for regularized image reconstruction,” *IEEE Transactions on Computational Imaging*, vol. 5, no. 3, pp. 395–408, 2019.
- [50] C. Paris, J. Bioucas-Dias, and L. Bruzzone, “A novel sharpening approach for superresolving multiresolution optical images,” *IEEE Transactions on Geoscience and Remote Sensing*, vol. 57, no. 3, pp. 1545–1560, 2019.
- [51] A. Teodoro, J. M. Bioucas-Dias, and M. A. T. Figueiredo, “Image restoration and reconstruction using targeted plug-and-play priors,” *IEEE Transactions on Computational Imaging*, 2019, doi:10.1109/TCI.2019.2914773.
- [52] T. Tirer and R. Giryas, “Image restoration by iterative denoising and backward projections,” *IEEE Transactions on Image Processing*, vol. 28, no. 3, pp. 1220–1234, 2019.
- [53] A. M. Teodoro, J. M. Bioucas-Dias, and M. A. Figueiredo, “A convergent image fusion algorithm using scene-adapted gaussian-mixture-based denoising,” *IEEE Transactions on Image Processing*, vol. 28, no. 1, pp. 451–463, 2018.
- [54] K. Zhang, W. Zuo, and L. Zhang, “Deep plug-and-play super-resolution for arbitrary blur kernels,” in *Proceedings of the IEEE Conference on Computer Vision and Pattern Recognition*, 2019, pp. 1671–1681.
- [55] K. Zhang, W. Zuo, S. Gu, and L. Zhang, “Learning deep CNN denoiser prior for image restoration,” in *Proceedings of the IEEE Conference on Computer Vision and Pattern Recognition*, 2017, pp. 3929–3938.
- [56] E. Ryu, J. Liu, S. Wang, X. Chen, Z. Wang, and W. Yin, “Plug-and-play methods provably converge with properly trained denoisers,” in *Proceedings of the International Conference on Machine Learning*, 2019, pp. 5546–5557.
- [57] S. Boyd, N. Parikh, E. Chu, B. Peleato, and J. Eckstein, “Distributed optimization and statistical learning via the alternating direction method of multipliers,” *Foundations and Trends® in Machine Learning*, vol. 3, no. 1, pp. 1–122, 2011.
- [58] M. V. Afonso, J. M. Bioucas-Dias, and M. A. T. Figueiredo, “An augmented lagrangian approach to the constrained optimization formulation of imaging inverse problems,” *IEEE Transactions on Image Processing*, vol. 20, no. 3, pp. 681–695, 2011.
- [59] J.-F. Cai, E. J. Candès, and Z. Shen, “A singular value thresholding algorithm for matrix completion,” *SIAM Journal on Optimization*, vol. 20, no. 4, pp. 1956–1982, 2010.
- [60] C. Lu, J. Feng, W. Liu, Z. Lin, and S. Yan, “Tensor robust principal component analysis with a new tensor nuclear norm,” *IEEE Transactions on Pattern Analysis and Machine Intelligence*, 2019, doi:10.1109/TPAMI.2019.2891760.
- [61] Z. Wang, A. C. Bovik, H. R. Sheikh, and E. P. Simoncelli, “Image quality assessment: from error visibility to structural similarity,” *IEEE Transactions on Image Processing*, vol. 13, no. 4, pp. 600–612, 2004.